Dynamic Visualization of Axial p–n Junctions in Single Gallium Nitride Nanorods under Electrical Bias

Yu-Jung Lu,[†,⊥] Ming-Yen Lu,[‡,⊥] Yu-Chen Yang,[†] Hung-Ying Chen,[†] Lih-Juann Chen,[§] and Shangjr Gwo[†,*]

[†]Department of Physics, National Tsing-Hua University, Hsinchu 30013, Taiwan, [‡]Graduate Institute of Opto-Mechatronics, National Chung-Cheng University, Chiayi 62102, Taiwan, and [§]Department of Materials Science and Engineering, National Tsing-Hua University, Hsinchu 30013, Taiwan. [⊥]Y.-J. Lu and M.-Y. Lu contributed equally to this work.

ABSTRACT We demonstrate a direct visualization method based on secondary electron (SE) imaging in scanning electron microscopy for mapping electrostatic potentials across axial semiconductor nanorod p–n junctions. It is found that the SE doping contrast can be directly related to the spatial distribution of electrostatic potential across the axial nanorod p–n junction. In contrast to the conventional SE doping contrast achieved for planar p–n junctions, the quasi-one-dimensional geometry of nanorods allows for high-resolution, versatile SE imaging under high accelerating voltage, long working distance conditions. Furthermore, we are able to delineate the electric field profiles across the axial nanorod p–n junction as well as depletion widths at different reverse biases. By using standard p–n junction theory and secondary ion mass spectroscopy, the carrier concentrations of p- and n-regions can be further extracted from the depletion widths under reverse biasing conditions. This direct imaging method enables determination of electrostatic potential variation of p–n junctions in semiconductor nanorod and nanowire devices with a spatial resolution better than 10 nm.

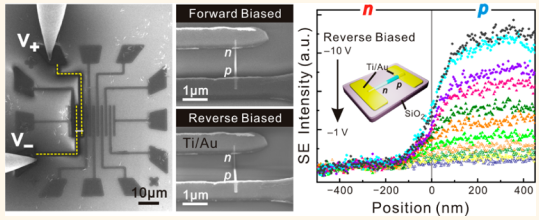

KEYWORDS: semiconductor nanowire · GaN nanorod · p–n junction · dopant profiling · secondary electron imaging · scanning electron microscopy

Semiconductor nanowires and nanorods have attracted much interest in the past decade due to their unique and tunable nature for nanophotonic and nanoelectronic applications.[1−7] It is believed that controlled synthesis, functionalization, and integration of these one-dimensional (1D) nanomaterials are likely to revolutionize nanoscience and nanotechnology.[5] Especially, 1D semiconductor heterostructures with well-defined geometries and modulated compositions have become of particular interest to achieve unique functionalities such as lasers,[2,3,5,6] light-emitting diodes,[8−10] solar cells,[11−13] sensors,[14] and field-effect transistors.[15,16] For most of these nanoscale device applications, it is indispensible to incorporate n- and p-type dopants into semiconductor nanostructures for the purposes of modulating their electrical properties and forming p–n junctions. In the previous studies, the formation of nanowire p–n junctions has been demonstrated by using the cross-wire[1,17] and coaxial (core–shell) nanowire[12,18,19] techniques. In the case where amphoteric doping for the same semiconductor is not possible, the heterostructure combinations of n-type (or p-type) nanowires with p-type (or n-type) nanowires or substrates have also been adopted to form p–n junction devices.[8,17] Recently, axially controlled modulation of doping and compositions along individual nanorods[9,10] or nanowires[20−22] has become a focused research area because of the increased versatility in device functionality, easy implementation of array-type devices,[9] and ultrasmall device footprint.[10] Here, we focus on gallium nitride (GaN) nanorod p–n junctions grown by plasma-assisted molecular-beam epitaxy (PAMBE). Vertically self-assembled GaN nanorod arrays have been demonstrated to be dislocation-free single crystals,[23] which can be used as strain-free growth templates due to their unique nanoscale geometry.[9] In addition, the $In_xGa_{1-x}N$ alloy is a direct band-gap semiconductor whose emission wavelengths can be tuned continuously with emission colors spanning from ultraviolet to the near-infrared region.[9,24] Most significantly for practical applications,

* Address correspondence to gwo@phys.nthu.edu.tw.

Received for review April 27, 2013 and accepted August 5, 2013.

Published online August 05, 2013
10.1021/nn4034986

contrary to other wide-band-gap semiconductor materials, GaN nanorods can be doped as both n- and p-type materials, which are a prerequisite for electrically driven photonic devices.

At present, the capability to delineate and quantitatively determine the electrostatic potentials and doping concentrations across the 1D semiconductor axial p−n junctions on the nanoscale is crucial for understanding the fundamental properties and improving nanorod and nanowire device performance. Besides conventional techniques such as secondary ion mass spectroscopy (SIMS) and capacitance−voltage measurements, a number of high-spatial-resolution dopant profiling techniques have been developed to fulfill the needs for next-generation semiconductor devices, which include electron holography,[25,26] secondary electron (SE) imaging in scanning electron microscopy (SEM),[27−34] scanning probe microscopies (*e.g.*, scanning Kelvin probe microscopy[35] and light-modulated scanning tunneling spectroscopy[36]), and synchrotron-radiation-based spectromicroscopy.[37] However, these techniques have not yet been demonstrated for studying nanowire and nanorod p−n junctions.

Recently, Garnett *et al.* demonstrated dopant profiling of single Si nanowires using the capacitance−voltage technique.[38] But the required high spatial resolution and direct electrostatic potential mapping for individual 1D nanostructures have not been demonstrated yet. Herein, we report a technique to perform dynamic visualization of electrostatic potential mapping for single semiconductor nanorod p−n junctions by *in situ* electrical measurements in SEM. It is found that the SE contrast can be directly observed across the axial nanorod p−n junction with sub-10 nm spatial resolution (which is governed by effective Debye length; please see details in the Supporting Information). Furthermore, the depletion widths and carrier concentrations of single GaN nanorod p−n junctions can be quantitatively determined.

RESULTS AND DISCUSSION

The GaN nanorod p−n junctions used in this study were grown by PAMBE.[23] Figure 1a shows a field-emission scanning electron microscopy (FESEM) image of a vertically aligned GaN nanorod p−n junction array with a visible SE doping contrast. The lengths of p- and n-type segments of GaN nanorods are about 1 μm, while the diameters of p- and n-GaN nanorod are 85 and 40 nm, respectively. The crystal structure of individual GaN nanorods was investigated by transmission electron microscopy (TEM) and scanning transmission electron microscopy (STEM) using a spherical-aberration-corrected 200 kV transmission electron microscope (JEOL JEM ARM200F). A bright-field STEM image and the corresponding diffraction pattern of single p−n GaN nanorod are shown in Figure 1b and c, respectively. Figure 1d is the high-resolution (HR) TEM image acquired from the interface of p- and n-GaN (marked area in Figure 1b). The separation of lattice fringes (0.52 nm) corresponds well to the lattice constant of bulk GaN along the wurtzite *c*-axis (⟨0001⟩ direction). These images reveal that PAMBE-grown GaN nanorods are single crystals with smooth surfaces

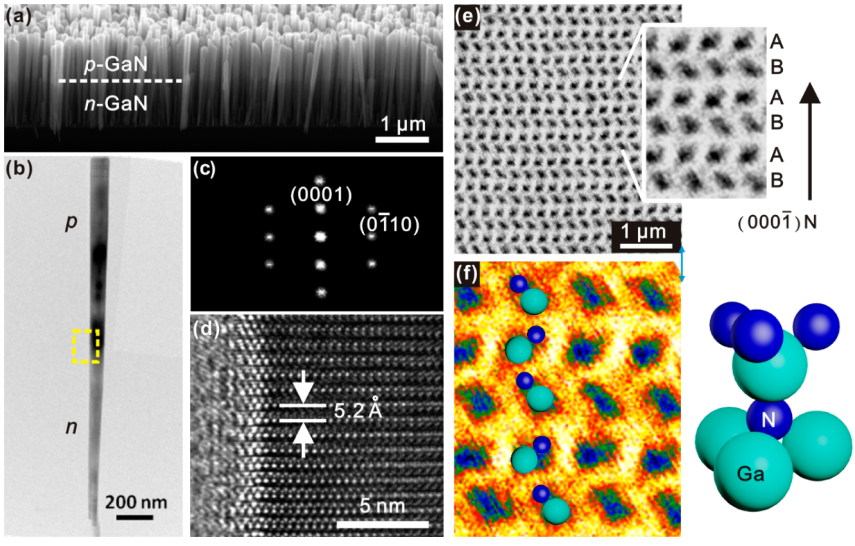

Figure 1. Morphological and structural characterization of GaN nanorods with axial p−n junctions. (a) Tilted FESEM image of PAMBE-grown GaN nanorod arrays. The p- and n- segments of nanorods are clearly visible in the image with bright and dark contrast, respectively. (b) Bright-field TEM image of a single GaN nanorod p−n junction. (c) Electron diffraction pattern of the p−n junction region exhibiting the single crystalline nature of a GaN nanorod. (d) High-resolution TEM image obtained at the p−n junction interface [marked area in (b)]. The measured lattice constant is about 5.2 Å, in good agreement with the known value of wurtzite GaN crystal along the ⟨0001⟩ direction. In addition, no defects are observed in the image, indicating that *as-grown* GaN nanorods are typically perfect crystal structures. (e) High-resolution annular bright field (ABF) STEM image of GaN nanorods showing the ABABAB stacking order of a wurtzite structure. (f) Magnified false-color ABF-STEM image illustrates that N atoms are on the top ends of Ga−N dumbbells, confirming the N-polarity of PAMBE-grown GaN nanorod.

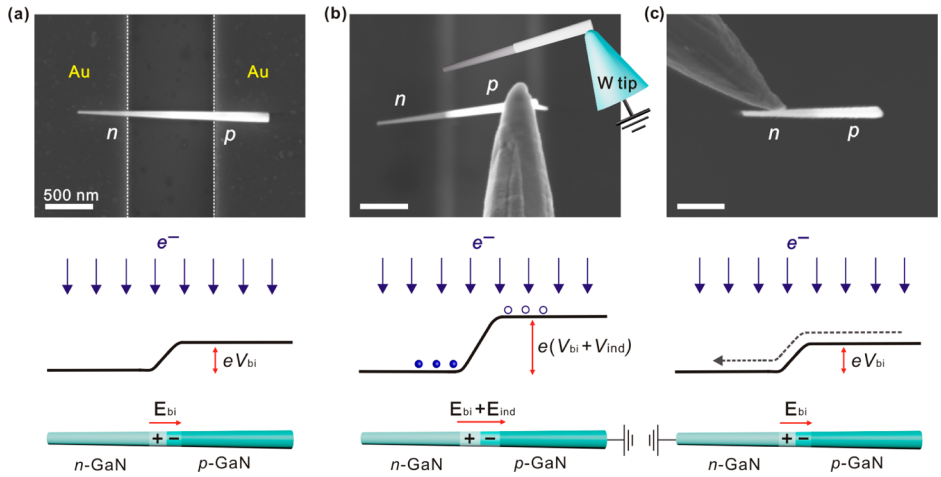

Figure 2. FESEM images of a single axial GaN nanorod p−n junction under different imaging conditions. (a) Weak imaging contrast acquired with the nanorod supported on unbiased Au electrodes at both sides. (b) In contrast, a significant imaging contrast arises when the nanorod is lifted to the free space using an electrically grounded probe tip at the p-type segment. (c) The imaging contrast of the freestanding GaN nanorod becomes weak by contacting the electrically grounded probe tip to the n-type segment. All the scale bars correspond to 500 nm. At the bottom of the FESEM images, the schematics show the variations of p−n junction band diagrams at different contact conditions. When the grounded tip contacts the p-type segment, the effective built-in potential becomes larger because of local charging of electrons at the n-type segment.

and the growth is along the *c*-axis. Also, excellent crystallographic alignment and defect-free nature are demonstrated in the HR-TEM image. As a consequence, the photoluminescence measurement of as-grown GaN nanorods exhibits only a sharp band-gap emission at 365 nm, and no significant defect emission peaks were detected (see Supporting Information Figure S3).

The atomic arrangement of p−n GaN nanorods was further investigated under aberration-corrected conditions. This technique provides direct imaging of both heavy and light elements at sub-angstrom resolution.[39] Figure 1e shows the annular bright-field (ABF) HR-STEM image of a GaN nanorod, revealing the ABABAB stacking order of wurtzite structure along the ⟨0001⟩ direction. The Ga−N dumbbell pairs are clearly visible in the magnified false-color image (Figure 1f), showing that N atoms are on top of the dumbbells and the PAMBE-grown GaN nanorods have nitrogen polarity.

The contrasts in the SEM vary with different doping concentrations, also known as doping contrast, was reported by Chang and Nixon as early as 1967.[27] In the SEM images, the SE collection from the p-type region is more than that from the n-type region; that is, the p-type region appears brighter than the n-type region in the SEM image. Later on, it was shown that the observed SE intensity not only depends on the doping type (n or p), but also varies quantitatively on the carrier concentrations in n- and p-type regions.[28] A linear relationship exists between the observed SE intensity and the logarithm of the carrier concentration of doped semiconductors in a wide range (over 4 orders of magnitude) of carrier concentrations.[29−32] This indicates that the escape barrier of SE in differently doped regions is the origin of the observed doping contrast. As a result, the SE intensity is proportional to the built-in electrostatic potential across the p−n junction.[30−32] In this work, we demonstrate significantly enhanced imaging contrast of single GaN nanorod p−n junctions under *in situ* electrical bias. All SE images were obtained by using a field emission SEM (Zeiss Ultra 55 FESEM) with an in-lens SE detector. The SE imaging conditions in our experiments are as follows: 15 kV accelerating voltage, 6 mm working distance, and ∼680 C/cm^2 electron dose, and the achievable spatial resolution is limited by the Debye length of GaN, which is <10 nm for the measured carrier concentrations (see Supporting Information for details). In order to understand the correlated SE variation of a nanorod p−n junction under electric bias, an *in situ* four-probe manipulation/measurement system was utilized for electrical measurements. We prepared the sharp tungsten probe tips by a wet chemical etching method, similar to the typical tip preparation method used for scanning tunneling microscopy. In particular, the surface depletion effects[40] are insignificant in this study by using a two-step surface treatment prior to the electrical measurements in SEM (see details in the Supporting Information). The SE doping contrast of planar semiconductor p−n junctions usually emerges under a low accelerating voltage of SEM (∼0.5−2 kV).[31] In comparison, the imaging contrast of GaN nanorod p−n junctions is significantly high, while the accelerating voltage in excess of 10 kV and a long working distance are used in in this work. These experimental conditions represent an important advantage of the SE imaging technique for electrostatic potential mapping of semiconductor nanostructure. It disclosed the high spatial resolution and the capability of biasing individual nanostucture p−n junctions by using an *in situ* nanoprobing stage.

To understand the contrast mechanism for individual GaN nanorods, we conduct a local charging experiment using an *in situ* nanomanipulation technique. Figure 2a shows the imaging contrast of a single GaN nanorod p−n junction supported on two unbiased electrodes at both ends, while Figure 2b and c show the free-standing cases with the ground probe tip holding p- and n-type nanorod segments, respectively. The corresponding p−n junction band diagrams show the electrostatic potential variations across the nanorod p−n junction, where $\mathbf{E}_{bi}$ and $\mathbf{E}_{ind}$ denote the built-in electric field and the local-charging-induced electric field, respectively. When a single GaN nanorod p−n junction is lifted to the free space from the p-GaN end using an electrically grounded tungsten tip (Figure 2b), the local charging at the n-GaN region occurs due to the built-in potential, and the trapped charge induces an opposite charge at the p-GaN region. In this situation, an internal electric field ($\mathbf{E}_{ind}$) is generated. As a result, the electrostatic potential difference between p- and n-GaN regions is significantly increased and a stronger SE image contrast across the junction can be observed. In comparison, Figure 2c indicates that no significant change in electrostatic potential occurs when the GaN nanorod is lifted to the free space by the grounded tip holding at the n-GaN end. The image contrast C_{pn} (*i.e.*, the SE doping contrast between p- and n-type regions) is defined by

$$C_{pn} = \frac{I_p - I_n}{I_p + I_n} \quad (1)$$

where I_p and I_n are the gray level intensities extracted from the SEM images of the p- and n-regions of GaN nanorod, respectively. The range of the gray level intensity value varies between 0 (black) and 255 (white). The image contrast is strongly dependent on the working distance at specific accelerating voltages.[34] Taking Figure 2b as an example, C_{pn} is found to be 36%, which is higher than that of previous studies for a planar p−n junction.[31,33] The present result indicates that enhanced imaging contrast from 1D semiconductor nanostructures arises from strong localized charging effects in low-dimensional nanostructures.

It is known that GaN p−n junctions with high crystalline qualities are expected to possess excellent electrical rectifier properties.[41−43] To measure the electrical properties of single GaN p−n junctions, we fabricated single GaN nanorod diode devices by using a photolithography process. An FESEM image of the fabricated device is shown in Figure 3a. *In situ* electrical measurements and imaging of single GaN nanorod p−n junction devices were carried out by contacting probes to metal electrodes in the FESEM, and the external biasing was performed by using a low-noise dc source (Keithley 2400). The electrical characteristic of a single GaN nanorod p−n junction is depicted in Figure 3b, and the inset is the schematic illustration of a single GaN nanorod diode device with Ti/Au electrodes. The Ti/Au

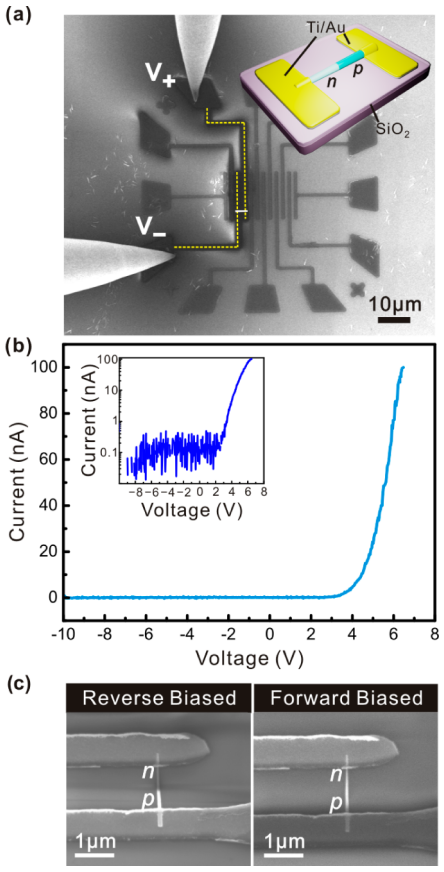

Figure 3. Electrical measurements were carried out in an FESEM equipped with a multiple-probe manipulation/measurement system. (a) FESEM image and schematics of the *in situ* measurement configuration. The yellow dashed lines in the image highlight the measuring electrodes with a single p−n GaN nanorod placed in between. (b) Electrical measurement for a single GaN nanorod p−n junction. The single GaN nanorod p−n junction exhibits rectifying characteristics in current−voltage measurement at room temperature. The inset shows a log-scale current−voltage plot showing that the reverse current is on the order of a picoampere at −10 V. (c) FESEM images of a single GaN nanorod p−n junction measured with a reverse and forward bias, respectively. The nanorod image shows a strong imaging contrast under reverse biasing conditions.

electrodes were used to form ohmic contacts on both the p- and n-side of the GaN nanorod.[44] The current−voltage plot is shown in log scale (as the inset of Figure 3b). It exhibits the typical rectifying behavior of a p−n junction with a clear turn-on voltage of 2.5 V. The ideality factor of a single GaN nanorod p−n junction is determined to be 12 at room temperature for the specific nanorod (see details in the Supporting Information), which has a similar value in comparison with the previous results (~6.5).[42] For the planar thin film p−n junction, the ideality factor is ~20.[45] The lower ideality factor of a single nanorod is attributed to being extended-defect-free in GaN nanorod p−n junctions. In particular, the reversed leakage current of a single GaN nanorod p−n junction remains very low (<10 pA) at −10 V, which is comparable to that measured from a dislocation-free GaN diode structure.[43] Interestingly, the

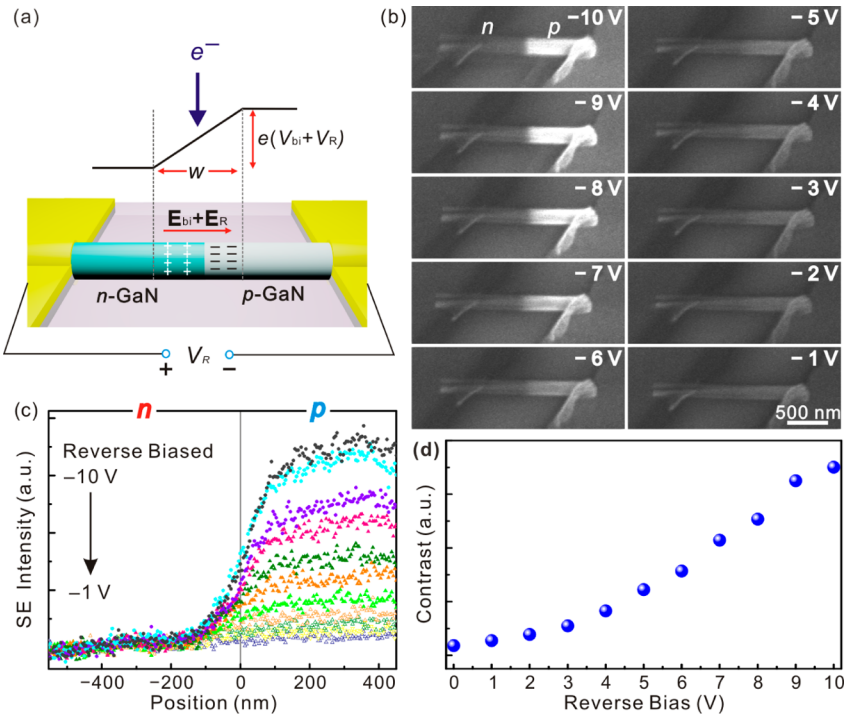

Figure 4. (a) Schematic illustration of the *in situ* measurement geometry. (b) Dynamic visualization of imaging contrast variation for a single GaN nanorod p−n junction. A sequence of FESEM images shows the electrostatic potential mapping variation for a single GaN nanorod p−n junction at different reverse biases (from −1 to −10 V). The dark and bright contrasts correspond to the n-GaN and p-GaN region, respectively. (c) Corresponding SE intensity line profiles along the nanorod derived from (b). (d) Plot of the SE intensity contrast between the p- and n-nanorod regions *versus* the applied reverse bias.

doping contrast of a single GaN nanorod p−n junction device varies significantly under different reverse biases, which are applied to enhance the effective built-in voltage.[31] The left and right SEM images in Figure 3c show doping contrast variation of a single GaN nanorod p−n junction under reverse and forward bias, respectively. This behavior can be well explained by the SE imaging contrast mechanism;[30−32] that is, forward biasing reduces the potential barrier across the p−n junction and reverse biasing increases the potential barrier.

Furthermore, the variation of imaging contrast across the *in situ* biased p−n junction can also be observed in real time by high-resolution SE imaging, which opens an interesting way to visualize the electrostatic potential variation of nanostructure p−n junctions at different biasing voltages. In this study, we find that the potential change for a single nanorod p−n junction can be clearly monitored and identified by the imaging contrast of a p−n junction in SEM images. Figure 4a shows the schematic diagram of the specimen geometry used for *in situ* electrical measurements, where V_{bi} is the built-in voltage, $\mathbf{E}_{bi}$ is the built-in electric field, W is the depletion width, and V_R and $\mathbf{E}_R$ are the reverse bias and the electric field induced by reverse bias, respectively. We performed *in situ*, real-time quantitative measurements of a single p−n GaN nanorod device under reverse biasing conditions. A sequence of high-resolution SE images acquired with reverse bias from 0 to −10 V is shown in Figure 4b, where the contrast variation results from different reverse bias conditions during the measurements. The corresponding intensity line profiles of the same nanorod at different reverse biases (extracted from Figure 4b) are plotted in Figure 4c. This plot clearly indicates that the change of SE contrast is due to the increase of effective built-in potential barrier at the p−n junction. Figure 4d shows the plot of the SE intensity variation between the p- and n-regions of the nanorod as a function of the applied reverse bias, illustrating that the electrostatic potential across the p−n junction increases with increasing reverse bias. The SE doping contrast can be extrapolated to zero at a forward bias of ~3 V, in line with the threshold voltage (2.5 V) exhibited in $I-V$ measurements.

The SE intensity from a semiconductor p−n junction has been known to correlate with the built-in electrostatic potential.[32] Therefore, the spatial distributions of electric field can be obtained by the first derivative of the SE intensity plot by using the following relationship:

$$\mathbf{E}(x) = -\mathrm{d}\phi(x)/\mathrm{d}x \qquad (2)$$

where ϕ and $\mathbf{E}$ represent the electrostatic potential and the electric field, respectively. The depletion widths at the space-charge regions can then be extracted by curve fitting of the experimental electric field profile (see details in the Supporting Information, Figure S4). Herein, the experimental results of the electric field plots under different reverse biases (from −6 to −10 V) are shown in

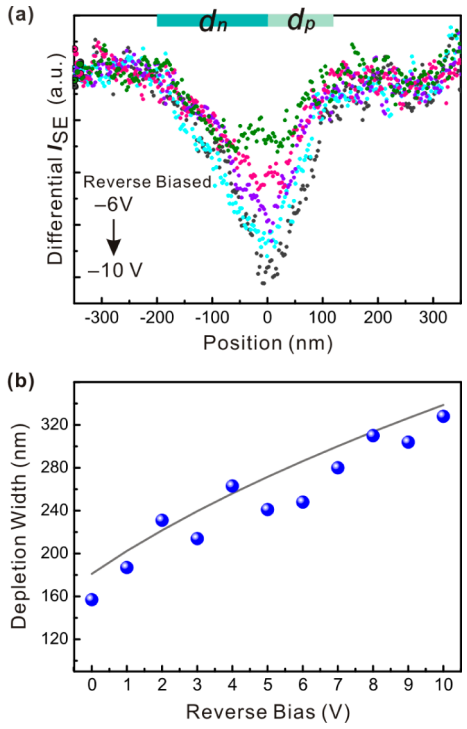

Figure 5. (a) Determination of depletion widths for a single GaN nanorod p−n junction. Electric field profiles derived from the measured SE intensity profiles under reverse bias (−6 to −10 V). The ratio of d_n/d_p remains the same at 2, where d_n and d_p correspond to the space charge width in the p-type and n-type GaN region, respectively. (b) Comparison of measured depletion widths (blue dots) and the standard p−n junction model. The solid curve shows the best fit of the standard p−n junction model.

Figure 5a. According to these results, the ratio of space charge width d_n/d_p remains about 2 for all biasing conditions, where d_n and d_p are the space charge widths at the n- and p-regions. This is reasonable since the depletion widths are fixed by the carrier concentrations and the charge neutrality condition. Figure 5b shows the plot of the depletion widths as a function of reverse bias, where the depletion widths range from 160 to 320 nm when the reverse bias is changed from 0 to −10 V. The depletion widths increase with increasing reverse bias across the junction. Using eqs 3 and 4, the curve shown in Figure 5b is the best fit using the standard p−n junction model, which has a good agreement with the experimental results.

$$W = \left\{ \frac{2\varepsilon_{GaN}(V_{bi} + V_R)}{e} \left[\frac{n+p}{n \times p} \right] \right\}^{1/2} \quad (3)$$

$$V_{bi} = \frac{kT}{e} \ln\left(\frac{n \times p}{n_i^2} \right) \quad (4)$$

where W represents the depletion width, e is electron charge, V_R is the reverse bias voltage, V_{bi} is the built-in voltage, ε_{GaN} is the dielectric constant of GaN, k is the Boltzmann constant, T is the temperature, n_i is the intrinsic carrier concentration (1.9×10^{-10} cm^{-3} for GaN at room temperature), and n and p are the carrier concentrations of n- and p-type GaN region, respectively. From the curve fitting, the carrier concentrations can be estimated as $p \approx 4 \times 10^{17}$ cm^{-3} for the p-GaN region and the built-in potential is 3.3 V. Since the ratio of space charge widths between n- and p-GaN is about 2, we can determine $n \approx 2 \times 10^{17}$ cm^{-3} for the n-GaN region. In order to confirm the carrier concentrations acquired from *in situ* electrical measurements, SIMS analysis was used to find that the concentration of magnesium (Mg) dopant in the p-type GaN nanorod region is about 2×10^{20} cm^{-3}. Mg has a large ionization energy (~180 meV), and typically less than 1% of Mg dopants are ionized.[46] According to our previous study, when the doping concentration of Mg in the nitrogen-polar GaN epitaxial layer was measured by SIMS to be $\sim 7 \times 10^{19}$ cm^{-3}, the carrier concentration of p-GaN was determined to be $\sim 1 \times 10^{17}$ cm^{-3} by Hall effect measurement.[37] It revealed that only 0.14% of Mg acceptors can be ionized. Thus, the carrier concentration of the p-GaN nanorod region can be estimated to be $p \approx 3 \times 10^{17}$ cm^{-3} by using the same activation ratio of Mg dopant. This is very close to the value measured by using the SE imaging technique.

CONCLUSIONS

In summary, we have demonstrated a high-resolution, direct electrostatic potential mapping method based on secondary electron imaging contrast in single semiconductor nanostructures. It is established that this imaging contrast can be directly related to the spatial distribution of electrostatic potential across the axial nanorod p−n junction. The key advantage for nanostructure characterization is that the electrostatic potential variation can be observed in real time under high-resolution imaging and *in situ* biasing conditions. Furthermore, the depletion widths and carrier concentrations can be quantitatively determined from secondary electron images. This technique is very useful to provide quantitative doping information for semiconductor nanostructure devices at the nanoscale.

MATERIALS AND METHODS

GaN Nanorod Growth Device Fabrication Procedure. The p−n GaN nanorods used in this study were grown on a 3 in., n-type Si(111) wafer by PAMBE. First, a 1 μm, n-type self-vertically aligned GaN nanorod array was grown on Si(111), and then a 1 μm, p-type GaN nanorod was grown on top of the n-type GaN nanorod. In order to fabricate the single nanorod device, the sample was dipped in 1% hydrogen fluoride (HF) solution for 30 s to remove the native oxide on the nanorods. We suspended nanorods in a 2-propanol solution using a sonic bath, and individual GaN nanorods were dispersed onto an oxidized (~500 nm in thickness) silicon substrate. The electrodes were patterned by a standard photolithography and lift-off technique. Both of the ohmic contacts to n- and p-type GaN were prepared by using

evaporated Ti/Au (20 nm/35 nm). Contact metals were prepared by electron-beam evaporation in a vacuum chamber, and the base pressure was in the 10^{-7} Torr range. After the contact fabrication process, nanorod devices were annealed under high vacuum at 600 °C for 20 s at a base pressure in the 10^{-9} Torr range.

***In Situ I–V* Measurements.** A Keithley 2400 souce-meter unit and a Zyvex S100 nanoprobing system were used for electrical measurements. The nanoprobing stage is installed in a field-emission scanning microscope (Zeiss Ultra 55), and the *I–V* measurements were performed at room temperature.

Conflict of Interest: The authors declare no competing financial interest.

Acknowledgment. This work was supported by research grants from the National Science Council (NSC) in Taiwan (NSC-102-2628-M-007-001, NSC-101-2628-M-007-006, NSC 102-2221-E-194-055, NSC-101-2218-E-194-002, and NSC-101-2221-E-007-078).

Supporting Information Available: Supporting figures and additional information. This material is available free of charge via the Internet at http://pubs.acs.org.

REFERENCES AND NOTES

1. Duan, X.; Huang, Y.; Cui, Y.; Wang, J.; Lieber, C. M. Indium Phosphide Nanowires as Building Blocks for Nanoscale Electronic and Optoelectronic Devices. *Nature* **2001**, *409*, 66–69.
2. Huang, M. H.; Mao, S.; Feick, H.; Yan, H.; Wu, Y.; Kind, H.; Weber, E.; Russo, R.; Yang, P. Room-Temperature Ultraviolet Nanowire Nanolasers. *Science* **2001**, *292*, 1897–1899.
3. Duan, X.; Huang, Y.; Agarwal, R.; Lieber, C. M. Single-Nanowire Electrically Driven Lasers. *Nature* **2003**, *421*, 241–245.
4. Ma, D. D. D.; Lee, C. S.; Au, F. C. K.; Tong, S. Y.; Lee, S. T. Small-Diameter Silicon Nanowire Surfaces. *Science* **2003**, *299*, 1874–1877.
5. Yang, P.; Yan, R.; Fardy, M. Semiconductor Nanowire: What's Next?. *Nano Lett.* **2010**, *10*, 1529–1536.
6. Yan, H.; Choe, H. S.; Nam, S.; Hu, Y.; Das, S.; Klemic, J. F.; Ellenbogen, J. C.; Lieber, C. M. Programmable Nanowire Circuits for Nanoprocessors. *Nature* **2011**, *470*, 240–244.
7. Lu, Y.-J.; Kim, J.; Chen, H.-Y.; Wu, C.; Dabidian, N.; Sanders, C. E.; Wang, C.-Y.; Lu, M.-Y.; Li, B.-H.; Qiu, X.; *et al.* Plasmonic Nanolaser Using Epitaxially Grown Silver Film. *Science* **2012**, *337*, 450–453.
8. Zhang, X.-M.; Lu, M.-Y.; Zhang, Y.; Chen, L.-J.; Wang, Z. L. Fabrication of a High-Brightness Blue-Light-Emitting Diode Using a ZnO-Nanowire Array Grown on *p*-GaN Thin Film. *Adv. Mater.* **2009**, *21*, 2767–2770.
9. Lin, H.-W.; Lu, Y.-J.; Chen, H.-Y.; Lee, H.-M.; Gwo, S. InGaN/GaN Nanorod Array White Light-Emitting Diode. *Appl. Phys. Lett.* **2010**, *97*, 073101.
10. Lu, Y.-J.; Lin, H.-W.; Chen, H.-Y.; Yang, Y.-C.; Gwo, S. Single InGaN Nanodisk Light Emitting Diodes as Full-Color Subwavelength Light Sources. *Appl. Phys. Lett.* **2011**, *98*, 233101.
11. Law, M.; Greene, L. E.; Johnson, J. C.; Saykally, R.; Yang, P. Nanowire Dye-Sensitized Solar Cells. *Nat. Mater.* **2005**, *4*, 455–459.
12. Tian, B.; Zheng, X.; Kempa, T. J.; Fang, Y.; Yu, N.; Yu, G.; Huang, J.; Lieber, C. M. Coaxial Silicon Nanowires as Solar Cells and Nanoelectronic Power Sources. *Nature* **2007**, *449*, 885–889.
13. Xu, J.; Yang, X.; Wang, H.; Chen, X.; Luan, C.; Xu, Z.; Lu, Z.; Roy, V. A. L.; Zhang, W.; Lee, C.-S. Arrays of ZnO/$Zn_xCd_{1-x}Se$ Nanocables: Band Gap Engineering and Photovoltaic Applications. *Nano Lett.* **2011**, *11*, 4138–4143.
14. Cui, Y.; Wei, Q.; Park, H.; Lieber, C. M. Nanowire Nanosensors for Highly Sensitive and Selective Detection of Biological and Chemical Species. *Science* **2001**, *293*, 1289–1292.
15. Liao, L.; Bai, J.; Cheng, R.; Lin, Y.-C.; Jiang, S.; Qu, Y.; Huang, Y.; Duan, X. Sub-100 nm Channel Length Graphene Transistors. *Nano Lett.* **2010**, *10*, 3952–3956.
16. Storm, K.; Nylund, G.; Samuelson, L.; Micolich, A. P. Realizing Lateral Wrap-Gated Nanowire FETs: Controlling Gate Length with Chemistry Rather than Lithography. *Nano Lett.* **2012**, *12*, 1–6.
17. Huang, Y.; Duan, X.; Cui, Y.; Lieber, C. M. Gallium Nitride Nanowire Nanodevices. *Nano Lett.* **2002**, *2*, 101–104.
18. Qian, F.; Li, Y.; Gradečak, S.; Wang, D.; Barrelet, C. J.; Lieber, C. M. Gallium Nitride-Based Nanowire Radial Heterostructures for Nanophotonics. *Nano Lett.* **2004**, *4*, 1975–1979.
19. Dong, Y.; Tian, B.; Kempa, T. J.; Lieber, C. M. Coaxial Group III–Nitride Nanowire Photovoltaics. *Nano Lett.* **2009**, *9*, 2183–2187.
20. Yang, C.; Zhong, Z.; Lieber, C. M. Encoding Electronic Properties by Synthesis of Axial Modulation-Doped Silicon Nanowires. *Science* **2005**, *310*, 1304–1307.
21. Lim, S. K.; Crawford, S.; Haberfehlner, G.; Gradečak, S. Controlled Modulation of Diameter and Composition along Individual III–V Nitride Nanowires. *Nano Lett.* **2013**, *13*, 331–336.
22. Hoffmann, S.; Bauer, J.; Ronning, C.; Stelzner, T.; Michler, J.; Ballif, C.; Sivakov, V.; Christiansen, S. H. Axial *p-n* Junctions Realized in Silicon Nanowires by Ion Implantation. *Nano Lett.* **2009**, *9*, 1341–1344.
23. Chen, H.-Y.; Lin, H.-W.; Shen, C.-H.; Gwo, S. Structure and Photoluminescence Properties of Epitaxially Oriented GaN Nanorods Grown on Si(111) by Plasma-Assisted Molecular-Beam Epitaxy. *Appl. Phys. Lett.* **2006**, *89*, 243105.
24. Kuykendall, T.; Ulrich, P.; Aloni, S.; Yang, P. Complete Composition Tunability of InGaN Nanowires Using a Combinatorial Approach. *Nat. Mater.* **2007**, *6*, 951–956.
25. Twitchett-Harrison, A. C.; Yates, T. J. V.; Newcomb, S. B.; Dunin-Borkowski, R. E.; Midgley, P. A. High-Resolution Three-Dimensional Mapping of Semiconductor Dopant Potentials. *Nano Lett.* **2007**, *7*, 2020–2023.
26. Midgley, P. A.; Dunin-Borkowski, R. E. Electron Tomography and Holography in Materials Science. *Nat. Mater.* **2009**, *8*, 271–280.
27. Chang, T. H. P.; Nixon, W. C. Electron Beam Induced Potential Contrast on Unbiased Planar Transistors. *Solid-State Electron.* **1967**, *10*, 701–702.
28. Perovic, D. D.; Castell, M. R.; Howie, A.; Lavoie, C.; Tiedje, T.; Cole, J. S. W. Field-Emission SEM Imaging of Compositional and Doping Layer Semiconductor Superlattices. *Ultramicroscopy* **1995**, *58*, 104–113.
29. Venables, D.; Jain, H.; Collins, D. C. Secondary Electron Imaging as a Two-Dimensional Dopant Profiling Technique: Review and Update. *J. Vac. Sci. Technol. B* **1998**, *16*, 362–366.
30. Sealy, C. P.; Castell, M. R.; Wilshaw, P. R. Mechanism for Secondary Electron Dopant Contrast in the SEM. *J. Electron. Microsc.* **2000**, *49*, 311–321.
31. Elliott, S. L.; Broom, R. F.; Humphreys, C. J. Dopant Profiling with the Scanning Electron Microscope—A Study of Si. *J. Appl. Phys.* **2002**, *91*, 9116–9122.
32. Kaestner, B.; Schönjahn, C.; Humphreys, C. J. Mapping the Potential within a Nanoscale Undoped GaAs Region Using a Scanning Electron Microscope. *Appl. Phys. Lett.* **2004**, *84*, 2109–2111.
33. Tsurumi, D.; Hamada, K.; Kawasaki, Y. Energy-Filtered Imaging in a Scanning Electron Microscope for Dopant Contrast in InP. *J. Electron. Microsc.* **2010**, *59*, S183–S187.
34. Jatzkowski, J.; Simon-Najasek, M.; Altmann, F. Novel Techniques for Dopant Contrast Analysis on Real IC Structures. *Microelectron. Reliab.* **2012**, *52*, 2098–2103.
35. Henning, A. K.; Hochwitz, T.; Slinkman, J.; Never, J.; Hoffmann, S.; Kaszuba, P.; Daghlian, C. Two Dimensional Surface Dopant Profiling in Silicon Using Scanning Kelvin Probe Microscopy. *J. Appl. Phys.* **1995**, *77*, 1888–1896.
36. Yoshida, S.; Kanitani, Y.; Oshima, R.; Okada, Y.; Takeuchi, O.; Shigekawa, H. Microscopic Basis for the Mechanism of Carrier Dynamics in an Operating *p-n* Junction Examined by Using Light-Modulated Scanning Tunneling Spectroscopy. *Phys. Rev. Lett.* **2007**, *98*, 026802.
37. Kuo, C.-T.; Lee, H.-M.; Shiu, H.-W.; Chen, C.-H.; Gwo, S. Direct Imaging of GaN *p-n* Junction by Cross-Sectional Scanning

Photoelectron Microscopy and Spectroscopy. *Appl. Phys. Lett.* **2009**, *94*, 122110.
38. Garnett, E. C.; Tseng, Y.-C.; Khanal, D. R.; Wu, J.; Bokor, J.; Yang, P. Dopant Profiling and Surface Analysis of Silicon Nanowires Using Capacitance–Voltage Measurements. *Nat. Nanotechnol.* **2009**, *4*, 311–314.
39. Ishikawa, R.; Okunishi, E.; Sawada, H.; Kondo, Y.; Hosokawa, F.; Abe, E. Direct Imaging of Hydrogen-Atom Columns in a Crystal by Annular Bright-Field Electron Microscopy. *Nat. Mater.* **2011**, *10*, 278–281.
40. Calarco, R.; Marso, M.; Richter, T.; Aykanat, A. I.; Meijers, R.; Hart, A. v. d.; Stoica, T.; Lüth, H. Size-Dependent Photoconductivity in MBE-Grown GaN-Nanowires. *Nano Lett.* **2005**, *5*, 981–984.
41. Cheng, G.; Kolmakov, A.; Zhang, Y.; Moskovits, M.; Munden, R.; Reed, M. A.; Wang, G.; Moses, D.; Zhang, J. Current Rectification in a Single GaN Nanowire with a Well-Defined *p*–*n* Junction. *Appl. Phys. Lett.* **2003**, *83*, 1578–1580.
42. Deb, P.; Kim, H.; Qin, Y.; Lahiji, R.; Oliver, M.; Reifenberger, R.; Sands, T. GaN Nanorod Schottky and p–n Junction Diodes. *Nano Lett.* **2006**, *6*, 2893–2898.
43. Kozodoy, P.; Ibbetson, J. P.; Marchand, H.; Fini, P. T.; Keller, S.; Speck, J. S.; DenBaars, S. P.; Mishra, U. K. Electrical Characterization of GaN *p-n* Junctions with and without Threading Dislocations. *Appl. Phys. Lett.* **1998**, *73*, 975–977.
44. Park, Y. S.; Park, C. M.; Park, C. J.; Cho, H. Y.; Lee, S. J.; Kang, T. W.; Lee, S. H.; Oh, J. E.; Yoo, K. H.; Son, M. S. Electron Trap Level in a GaN Nanorod *p-n* Junction Grown by Molecular-Beam Epitaxy. *Appl. Phys. Lett.* **2006**, *88*, 192104.
45. Motayed, A.; Davydov, A. V.; Vaudin, M. D.; Levin, I.; Melngailis, J.; Mohammad, S. N. Fabrication of GaN-based Nanoscale Device Structures Utilizing Focused Ion Beam Induced Pt Deposition. *J. Appl. Phys.* **2006**, *100*, 024306.
46. Romano, L. T.; Kneissl, M.; Northrup, J. E.; Van de Walle, C. G.; Treat, D. W. Influence of Microstructure on the Carrier Concentration of Mg-Doped GaN Films. *Appl. Phys. Lett.* **2001**, *79*, 2734–2736.